Draft version November 3, 2023
Typeset using LaTeX **twocolumn** style in AASTeX631

Magnetic fields and plasma heating in the Sun's atmosphere

P. Judge [1], L. Kleint [2], R. Casini [1], A.G. de Wijn [1], T. Schad [3] and A. Tritschler [4]

[1] *High Altitude Observatory, National Center for Atmospheric Research, Boulder CO 80307-3000, USA*
[2] *University of Bern, Astronomical Institute, Sidlerstrasse 5, 3012 Bern, Switzerland*
[3] *National Solar Observatory, 22 ´Ohi´a Kū Street, Pukalani, HI 96768, USA*
[4] *National Solar Observatory, 3665 Discovery Drive, Boulder CO 80303, USA*

(Dated: Accepted . Received ; in original form)

ABSTRACT

We use the first publically available data from the Daniel K. Inouye Solar Telescope (DKIST) to track magnetic connections from the solar photosphere into the corona. We scrutinize relationships between chromospheric magnetism and bright chromospheric, transition region and coronal plasmas. In June 2022, the Visible Spectro-Polarimeter (ViSP) instrument targeted unipolar network within a decaying active region. ViSP acquired rastered scans with longitudinal Zeeman sensitivities of 0.25 Mx cm^{-2} (Fe I 630.2 nm) and 0.5 Mx cm^{-2} (Ca II 854.2 nm). ViSP was operated in a "low" resolution mode (0.214″ slit width, spectral resolution $\mathcal{R} \approx 70,000$) to produce polarization maps over a common area of 105″ × 50″. Data from SDO and IRIS are combined to ask: Why is only a fraction of emerging flux filled with heated plasma? What is the elemental nature of the plasmas? No correlations were found between heated plasma and properties of chromospheric magnetic fields derived from the WFA, on scales below supergranules. Processes hidden from our observations control plasma heating. While improved magnetic measurements are needed, these data indicate that "the corona is a self-regulating forced system" (Einaudi et al. 2021). Heating depends on the state of the corona, not simply on boundary conditions. Heating models based upon identifiable bipolar fields, including cool loops, tectonics and observable magnetic reconnection, are refuted for these regions with unipolar chromospheric magnetic fields.

Keywords: Spectropolarimetry (1973); Solar corona (1483); Solar transition region (1532); Solar chromosphere (1479)

1. INTRODUCTION

In the absence of sufficiently sensitive measurements of magnetic fields directly beneath the corona, speculations abound concerning the predominant physical processes responsible for the structure and heating mechanisms of the overlying plasmas. Magnetic fields penetrating from beneath the solar surface have been established as the agent responsible for heating the chromosphere and corona, and the plasma at intermediate temperatures (Howard 1959; Leighton 1959; Reeves 1976; Schrijver et al. 1985; Schrijver 1987, 1988; Schrijver & Harvey 1989; Cook & Ewing 1990; Neupert 1998; Fisher et al. 1998; Schrijver et al. 1998; Gallagher et al. 1998; Mandrini et al. 2000; Martinez-Galarce et al. 2003; Schrijver & Title 2003; Doschek et al. 2004; Loukitcheva et al. 2009; Parnell & de Moortel 2012; Schmelz & Winebarger 2015; Ayres 2021; Toriumi & Airapetian 2022; Aschwanden & Nhalil 2023). Among many others including stellar work, these studies document correlations between magnetic fields, plasma emission from chromosphere, transition region and corona. While exceptions exist (see, for example the introduction of the paper by Chitta et al. 2021), the bulk of the observational analyses generally find strong correlations. The current paradigm requires that magnetic fields are necessary for significant plasma heating, but that not all magnetic fields threading the atmosphere lead to plasma heating.

These results have prompted various proposals for magnetic heating mechanisms, such as the resonant development and dissipation of internal surface waves (e.g. Ionson 1978), phase mixing (Heyvaerts & Priest 1983; Mok & Einaudi 1990; Howson et al. 2019) and small scale magnetic reconnection exhibited in the form of small flares (Parker 1988, 1994), driven perhaps by turbulence (Rappazzo et al. 2008). But an unfortunate as-

Corresponding author: P. Judge

pect of current understanding is that multiple solutions to the coronal heating problem remain actively in contention (e.g. Aschwanden 2001; de Pontieu et al. 2021; Pontin & Priest 2022), despite decades of coronal observations and advances in computation (Judge & Ionson 2023). Other elementary difficulties still challenge our understanding. For example, although called "transition region" plasmas, the plasmas responsible for the bulk of the emission between 10^4 and 10^6 K may not necessarily form a physical transition between warm and hot plasma (contrast the perspectives of Feldman 1983; Dowdy et al. 1986; Hansteen et al. 2014 and Judge 2021). The inability of classical heat conduction from the corona to account for this "transition region" emission below 10^5 K (see, e.g., Cally 1990), including the dominant line of H Lα, has prompted authors for over three decades to look for other explanations (Mariska 1992; Judge 2021). One idea has proven resilient, namely that a host of unresolved loops lie within supergranular cell "lanes" (Dowdy et al. 1986), regions of magnetic fields accumulated as granular-scale magnetic structures are advected by horizontal supergranular flows to these lanes. Interaction with the pre-existing flux leads to bright emission from rapidly evolving small bipolar loops (Dowdy et al. 1986), and to the development of embedded current sheets, which when dissipated are also a source for heating the overlying corona (Priest et al. 2002). Hansteen et al. (2014), using the IRIS instrument (de Pontieu et al. 2014), were able to resolve some cool loops in observations near the solar limb. However, Judge (2021) argued that cool loops are not abundant enough to account for transition region emission in the quiet Sun.

Our goal is to study observationally how plasma heating is related to magnetic structure measured in the photosphere and chromosphere obtained using the ViSP instrument (de Wijn et al. 2022) at the Daniel K. Inouye Solar Telescope (DKIST: Rimmele et al. 2020). Novel aspects include not only chromospheric magnetic fields, but also velocity fields, all compared at the highest angular resolution and sensitivity with accurately co-aligned heated plasmas from chromosphere to corona. We will show that the correlations break down when scrutinized in such detail. Since magnetic energy is converted to heat only on small, unresolved scales, we will argue that the generally accepted paradigm for coronal heating may need modifying to be consistent with these new and revealing results.

2. OBSERVATIONS

2.1. *VISP data*

The data were obtained during a joint campaign with Parker Solar Probe (Fox et al. 2016). The region observed and reported here was assigned the number NOAA 13066 on 5 May 2022. Classified according to the scheme of Giovanelli (1982), this is an unusually unipolar region. More typical "unipolar" regions exhibit a ratio of dominant to subdominant polarity near 9:1, not 50:1 as measured here by ViSP. AIA images (Lemen et al. 2012) from the SDO spacecraft (Pesnell et al. 2012) reveal network that is brighter than average, lying at the leading (westward) edge of the plage arising from the breakup of NOAA 13006. This work builds on that of Judge & Centeno (2008) by including measurements of chromospheric magnetic fields in the Ca II 854.2 nm line as well as the photospheric Fe I 630.2 nm line pair. These data are augmented with simultaneous data from instruments on SDO, and data from the IRIS instrument obtained before and after the DKIST scans.

The DKIST targeted chromospheric network (Hale & Ellerman 1904) within the remnant of NOAA 13006, highlighted in Figures 1 and 2. The DKIST experiment ID was eid_1_118. Here we highlight data obtained with arms 1 and 3 of the ViSP spectrograph, with cameras centered at 603.2 and 854.2 nm (see Table 1), for one scan that began near 17:39 UT on 3rd June 2022, a period of very good seeing. Arm 2 of the spectrograph was not used. The Table includes all observations analyzed in our study, and pairs together data from the two arms, each of which has its own geometry as listed in the central solar coordinates $(x_{\rm cen}, y_{\rm cen})$ spatial pixel sizes (dx, dy), and rotation angle. The field of view for arm 1 was $105'' \times 77''$, while for arm 2 it was $105'' \times 50''$ because of different magnifications at the image planes. We present and analyze data from DKIST level 1 datasets labeled BRWJV and AVORO. They represent data typical of all scans, selected because of a more uniform quality of seeing. The two wavelength regions contain Zeeman-sensitive spectral lines of Fe I and Ca II formed in the photosphere and mid-chromosphere respectively. ViSP was operated in full spectropolarimetric mode. It recorded linear combinations of Stokes parameters $I_\lambda, Q_\lambda, U_\lambda, I_\lambda$ with time, parameters which measure intensity I, two states of linear polarization (Q, U) and circular polarization (V, see chapter 1 of Landi degl'Innocenti & Landolfi 2004, for definitions of the Stokes parameters).

Each scan used the largest available ViSP slit at the spectrograph entrance, subtending an angle of $0\farcs214$, with a slit-limited resolution of $0\farcs428$ ($\approx$ 300 km at the Sun's surface), along the solar X direction (E-W). The slit was oriented in the solar N-S direction, and was moved across the solar image in steps of a full slit-width between integrations. Below we will find that the resolution measured along the slit (N-S, solar Y direction) is also $\approx 0\farcs4$. At each slit position the instrument measured the full state of polarization of the incoming light, by recording intensities at 10 equally spaced angular positions of the continuously rotating modulator. The frame rate was 41.357 Hz, and the exposure times were 4.0 ms for both cameras. Thus the camera duty cycle was $\approx 16.5\%$. For arm 1 an attenuation filter with an optical density of 0.6 was inserted in the beam. For each slit position, the modulation cycle was repeated

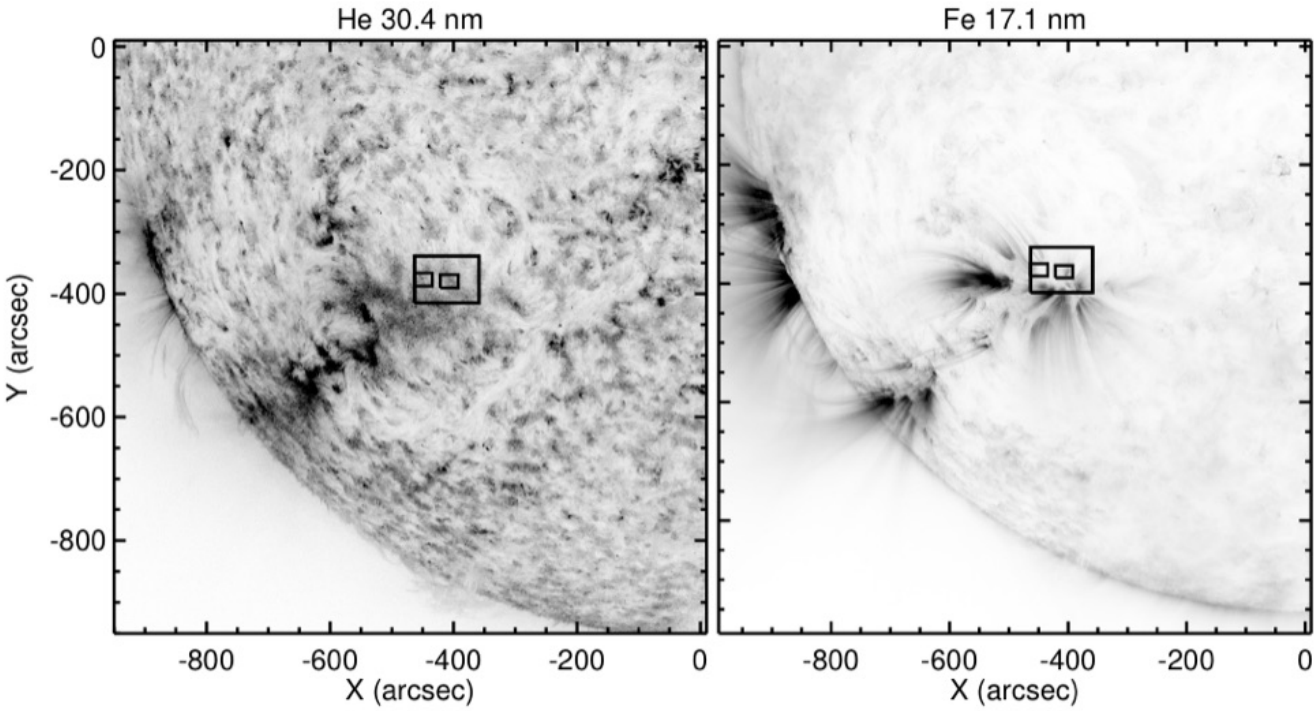

Figure 1. The SE quadrant of the Sun is shown as a sum of images obtained at 30.4 nm ("transition region") and 17.1 nm (corona) on June 3 2023. An inverse color scale is used. Rectangular regions of interest are shown in more detail in Figure 2

.

Table 1. Parameters of ViSP observations on 2022-06-02 and 2022-06-03

ID	λ	mid-scan time	$x_{\rm cen}$	$y_{\rm cen}$	dx	$dy^\dagger$	rotation	nearest IRIS
			arc seconds				clockwise deg.	SJI mid time
AODMM	630	2-Jun-2022 20:02:23	-494.7	-405.0	0.2130	0.0594	-0.1	17:54
APJND	854	20:02:23	-494.5	-410.1	0.2126	0.0388	-0.15	17:54
BRWJV	630	3-Jun-2022 17:52:23	-411.1	-377.0	0.2128	0.0594	-0.18	16:58
AVORO	854	17:52:23	-410.5	-381.9	0.2124	0.0388	-0.23	16:58
AWOWP	630	17:23:21	-416.4	-436.2	0.2090	0.0594	-0.15	16:58
AXVLY	854	17:23:21	-415.6	-441.0	0.2081	0.0387	-0.20	16:58
BPJDD	630	18:21:07	-311.7	-377.0	0.2120	0.0594	-0.10	20:04
BQKZZ	854	18:21:07	-311.3	-382.1	0.2120	0.0389	-0.02	20:04
BNKVM	630	18:49:52	-312.5	-434.3	0.2137	0.0600	-0.10	20:04
BODXM	854	18:49:52	-312.0	-439.5	0.2135	0.0383	-0.05	20:04

Pixel sizes dx, dy and rotations of the ViSP images are those derived from the alignment with the HMI data. The ViSP scans took 26 minutes, IRIS scans were 14 minutes in length. †These values of the pixel size along the solar Y direction have been binned by a factor of two, i.e. they are twice those of the original data.

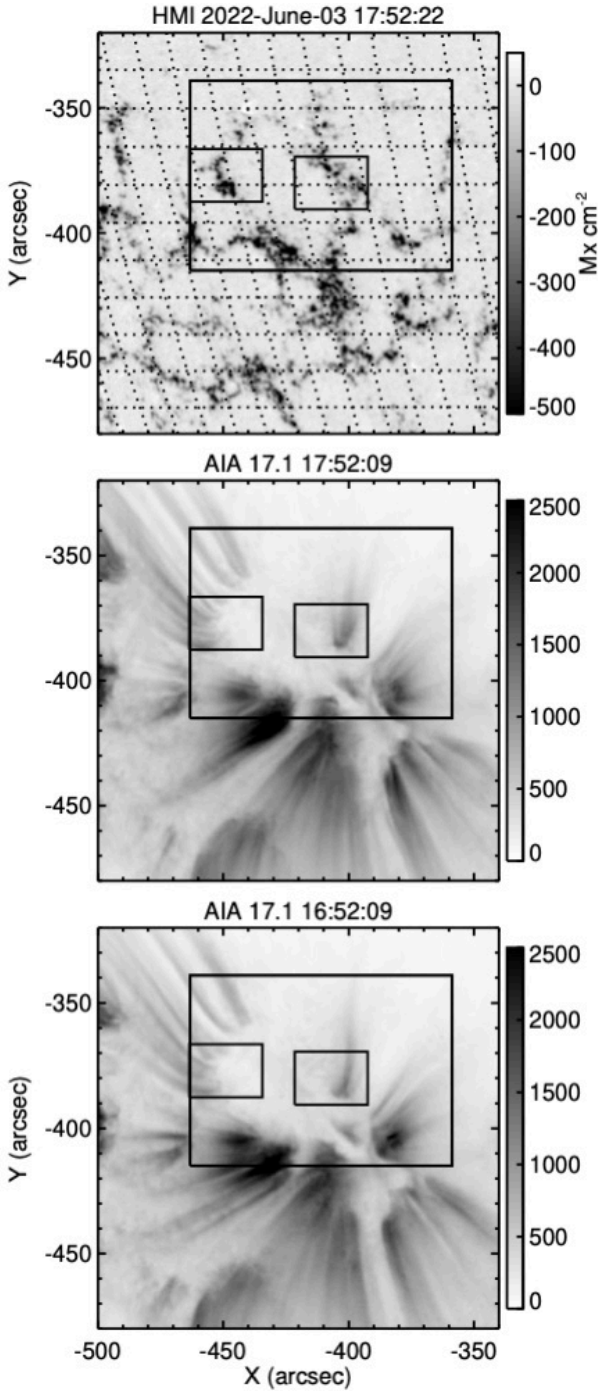

Figure 2. The area observed by arm 1 of the ViSP is shown by the large black box. The images show line of sight magnetic fields and coronal data from the SDO spacecraft. The small boxes show regions discussed in more detail. The AIA data at 17.1 nm were acquired 1 hour apart to illustrate the typical evoluton of plasma loops, at 16:52 and at 17:52 UT on June 3 2022.

12 times (6 full rotations of the modulator), and each of the 10 modulated signals was co-added over the 12 cycles. The ViSP performs dual-beam polarimetry to reduce seeing-induced crosstalk (e.g., Lites 1987), and records the two beams of orthogonal polarization on the same detector. The instrument performance model, verified using science verification data for the 0.″041 slit, predicts spectral resolutions of 76,000 (630.2 nm) and 69,000 (854.2 nm) for the 0.″214 slit.

2.2. *Alignment of different datasets*

At the level of accuracy required below, alignment between various instruments required great care. We adopt the coordinate frame defined by the line-of-sight (LOS) field components from the Stokes V measurements of the HMI instrument (Hoeksema et al. 2018), against which all images were co-aligned.

Line-of-sight magnetograms constructed from the level 1 ViSP data were aligned to better than $\approx 0.3''$, by eye. These alignments required modest image stretching and rotation, as well as centering, and were done for photospheric lines in each ViSP camera, thus removing any image shifts by differential refraction. More precise determinations were precluded by the fact that the ViSP is a scanning slit instrument, and the Stokes V_λ signals evolved during the 26 minute ViSP scan times. A higher precision was found to be unnecessary for our purposes *post-facto*, and so more refined co-alignments of HMI and ViSP data were not attempted.

The geometric ViSP pixel sizes inferred from this alignment (listed in Table 1) are within 1% of those in the VISP level 1 headers. Along the slit (i.e., in the solar Y-direction), angular resolution is set by the telescope system's imaging performance, as well as seeing. The nominal pixel sizes along the slit are 0.″0294 and 0.″0194 for arms 1 and 3 (630.2 and 854.2 nm) respectively, smaller than the slit width by factors of 7.4 and 11 respectively. Given these rates of over-sampling, we re-binned data along the slit direction into pixels a factor of two larger before proceeding, to handle the many images more quickly during processing. The larger bin sizes used, determined from the alignment with HMI, are listed in Table 1. The alignment quality can be partly assessed using Spearman cross-correlation coefficients, which are listed in Table 2.

The angular resolution along the ViSP slit was estimated from power and phase-difference spectra of intensity, which show coherent power on all scales up to $\approx 0.15\times$ the Nyquist frequency ($\mathcal{N} = 0.5/dy$). This corresponds to a full width at half maximum of the point spread function—the effective angular resolution—of $\approx$ 0.″4. The ViSP Feed-Optic telescope that focuses the DKIST incoming beam onto the spectrograph's slit was later discovered to be slightly out of focus after this campaign, limiting the spatial resolution achievable. Somewhat fortuitously, this happened to be close to the sampling-limited resolution along the orthogonal

Table 2. Spearman's rank correlation coefficients over small areas (10 Mm) of BRWJV and AVORO

	$B^{854}_{\rm LOS}$	$B^{854}_{\rm POS}$	160	170	279	133	140	30.4	13.1	17.1	19.5	21.1	33.5
$B^{630}_{\rm LOS}$	0.49	0.01	**0.79**	**0.80**	0.15	0.06	0.06	0.13	0.08	-0.13	-0.19	-0.17	0.08
$B^{854}_{\rm LOS}$		0.01	**0.50**	0.46	0.33	0.06	0.13	0.40	0.06	-0.11	-0.25	-0.26	-0.01
$B^{854}_{\rm POS}$			0.06	0.05	0.12	0.07	0.06	0.10	0.06	0.09	0.06	0.09	0.04
160				**0.95**	0.33	0.22	0.21	0.26	0.16	-0.05	-0.14	-0.09	0.11
170					0.25	0.17	0.17	0.21	0.09	-0.12	-0.21	-0.15	0.07
279						**0.63**	**0.61**	**0.62**	**0.57**	**0.51**	0.30	0.42	0.39
133							**0.79**	0.31	0.44	0.31	0.18	0.31	0.33
140								0.32	0.48	0.37	0.27	0.35	0.36
30.4									0.28	0.12	-0.07	-0.01	0.17
13.1										**0.71**	**0.70**	**0.68**	**0.80**
17.1											**0.91**	**0.94**	**0.53**
19.5												**0.95**	**0.55**
21.1													**0.52**

Rank correlation coefficients above 0.5 are in boldface. The coefficients in rows and columns for 279, 133 and 140 were computed from contemporaneous IRIS data obtained near 16:51 UT. The other values were computed using data obtained close to 17:52 UT. Small correlation coefficients of 0.33 and 0.30 are found between SDO 30.4 and IRIS 133 and 140 nm features obtained 55 minutes apart, evolving significantly (Figure 6), suggesting that values of $\lesssim 0.3$ indicate insignificant correlation.

X-direction ($0\farcs428$), thus the images appear consistent with a symmetric PSF.

Data from SDO HMI and AIA instruments were acquired with their nominal cadence throughout the DKIST scan. Only the "45s" longitudinal magnetic field from HMI was used, used only to provide a reference frame for all observations. Two different methods were used to align EUV and UV data to the HMI reference frame. For AIA, we found Sun center through optimal correlations of the entire field of view of each image with the 2D Gaussian function $\exp(-r^2/r^2_\odot)$. For IRIS, we then performed a cross-correlation for the overlapping field of view of the 160 nm AIA images with those of IRIS. These alignments are $\pm 1''$ or better. The coefficient for rank cross-correlation between HMI $B_{\rm LOS}$ and AIA 160 nm listed in Table 2 is 0.68, increasing to 0.80 for the 170 nm band formed in the upper photosphere (Vernazza et al. 1981).

The final column in Table 1 shows the start times of the nearest IRIS scans because no simultaneous measurements were made with the ViSP scans. Each IRIS scan ran for 14 minutes. Of these, the two DKIST scans AWOWP/AXVLY and BPJDD/BQKVV began within half an hour of the IRIS scans. Nevertheless, we focus here on BRWJV/AVORO because of the higher quality seeing conditions. This means that we will examine the three IRIS data products (133, 140 and 279 nm slitjaw images, dominated by emission from lines of C II, Si IV and Mg II respectively) obtained an hour before the DKIST scans began. The correlations reported in Table 2 are from simultaneous data from SDO and IRIS, and from simultaneous data from SDO and ViSP. Those between ViSP and IRIS are *not* simultaneous measurements, the effects of this mis-match are discussed below.

It is important to stress that image alignments better than $1''$ proved possible only for morphologically similar images, such as AIA 13.1, 17.1, 19.3 images, HMI and DKIST magnetograms and AIA 170 and 160 images, and IRIS slitjaw images at 133, 140 and 279 nm images with AIA 170 nm. The accuracy of alignments of the EUV AIA data with all other data are therefore subject to larger errors of $\approx \pm 2 - 3''$. These uncertainties were estimated by comparison between the values derived above with a careful manual alignment using particular features across the solar disk. Of our conclusions, none is affected by these problems, because no refinements of the alignments alter the lack of correlations which is the novel finding of this study, even for mis-alignments $\gtrsim 5''$ (compare, e.g., variations of $B_{\rm LOS}$ with those of 17.1 emission shown in Figures 5, 7).

2.3. *UV and EUV data*

In our analysis of EUV data from the AIA instrument on SDO, we averaged ten exposures obtained from 17:51 to 17:53 UT to enhance signal-to-noise ratios (Figure 2), during which time the solar images rotated by less than $0\farcs3$. Figure 3 shows images from the transition region to the corona. The morphology of coronal emission remains similar for all coronal images, the plasmas emitting in the same fashion at the temperatures typically sampled by these data. These data were augmented with slitjaw images from IRIS, which scanned the same region, but only before and after the DKIST scans. IRIS was unfortunately pointed to a different active region during

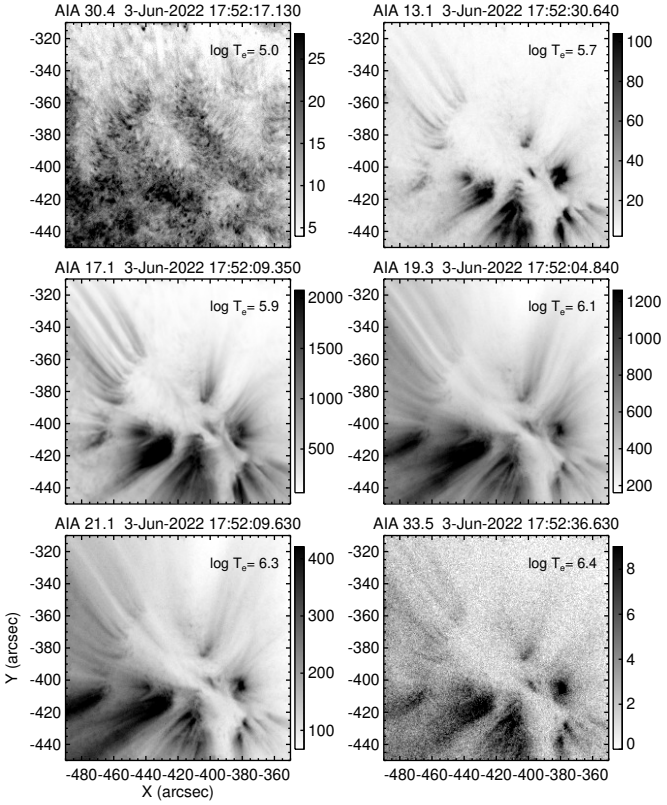

Figure 3. Images of UV and EUV emission from the AIA instrument are shown, obtained close to the center of the ViSP raster scan. Each image is a sum of several images between 17:50 and 17:53 UT. Intensity scales are average data numbers.

the DKIST scan with mid-time 17:52:23 UT, but IRIS data are available from 16:50:56.700 to 17:05:37.760 UT, ending 41 minutes before the start of the DKIST scan. In the figures these IRIS data were obtained between 16:51 and 17:10 UT, but were rotated to 17:52 UT for direct comparison with the other images. Further IRIS scans only began after 19:57 UT on 23 June 2023.

Figures 4 and 6 show close-up views of DKIST magnetic and intensity data in comparison with the AIA data, allowing us to relate transition region emission in the He II 30.4 nm line to be assessed relative to the overlying corona as well as underlying magnetic fields. A well-known but weak blend within the 30.4 nm bandpass of AIA includes a line of Si XI, whose emission should be similar to the AIA images of Fe XII at 17.1 nm shown. Included in Figures 4 and 6 are slitjaw images obtained by the IRIS instrument in C II at 133 nm, those of Si IV (not shown) are morphologically very similar. lines, both formed in the lower transition region.

In these figures, the IRIS images, obtained over 45 minutes before the DKIST scan, are compared with simultaneous AIA data at 30.4 nm as well as data obtained during the ViSP scan. The sequence of 24 slitjaw images acquired by IRIS between 16:51 and 17:05 reveals time-dependent changes typical of other solar regions (e.g., Skogsrud et al. 2015). The 30.4 nm panels of Figures 4 and 6 show that the morphology of the IRIS C II images at 133 nm are quite different. Mg II 279 and Si IV 140 nm data (not shown) are morphologically similar to those at 133 nm. Under standard assumptions of the formation of these EUV lines (Lang et al. 1990), these enormous differences are not possible, and the morphology would be similar on all observed scales. The implications of such radical departures from theories of line formation as well as models for energy transport though the "transition region" will be speculated upon below.

Variations of coronal images on June 3rd 2022 are far less dramatic than those observed in transition region plasmas, the 1 hour differences being highlighted in the AIA 17.1 images of Figure 2. The individual plasma loops persist within at least two of three images acquired at 17:29, 17:52 and 18:29 UT, slowly coming and going within the same magnetic structure. This is consistent with a slow thermal cooling time of 10-20 minutes (e.g Kuin & Martens 1982).

Figures 5 and 7 show slices through some of the images of Figures 4 and 6 respectively, reinforcing the above statements, and showing quantitatively the remarkable differences between properties of photospheric, chromospheric, transition region and coronal plasmas. These differences are plainly evident even at the angular resolution of the EUV SDO images, which is at best 1″, compared with 0.″4 for the ViSP data.

2.4. *Chromospheric velocity fields from DKIST data*

Using the intensity profiles of the Ca II line, we derived line-of-sight velocity shifts $v_{\rm LOS}$ and line widths $w_{\rm LOS}$ in two ways. We are mostly concerned with conditions at the base of the corona, and so we focus on the Ca II line at 854.2 nm.

Shifts were derived from fits to the absorption line profiles using Gaussian functions. These were checked against finding the spatial average of all profiles and finding the maximum cross-correlation of each profile with the average, measured in pixels, and using a parabola to find the peak of the cross-correlation function. Both derivations yield values close to the central wavelength of the line cores, the minimum in intensity.

The non-thermal Doppler width ξ, will be used below to estimate Poynting fluxes entering the corona:

$$\xi = \sqrt{w_{\rm LOS}^2 - \frac{kT}{A\,m_{\rm H}} - s^2} \quad {\rm cm\ s^{-1}}. \qquad (1)$$

Here, $w_{\rm LOS}$ is the Doppler line width (i.e., the measured full width at half-maximum line depth divided by $2\sqrt{\ln 2}$), k is Boltzmann's constant, A the atomic mass of the radiating ion, $m_{\rm H}$ is the mass of a hydrogen atom,

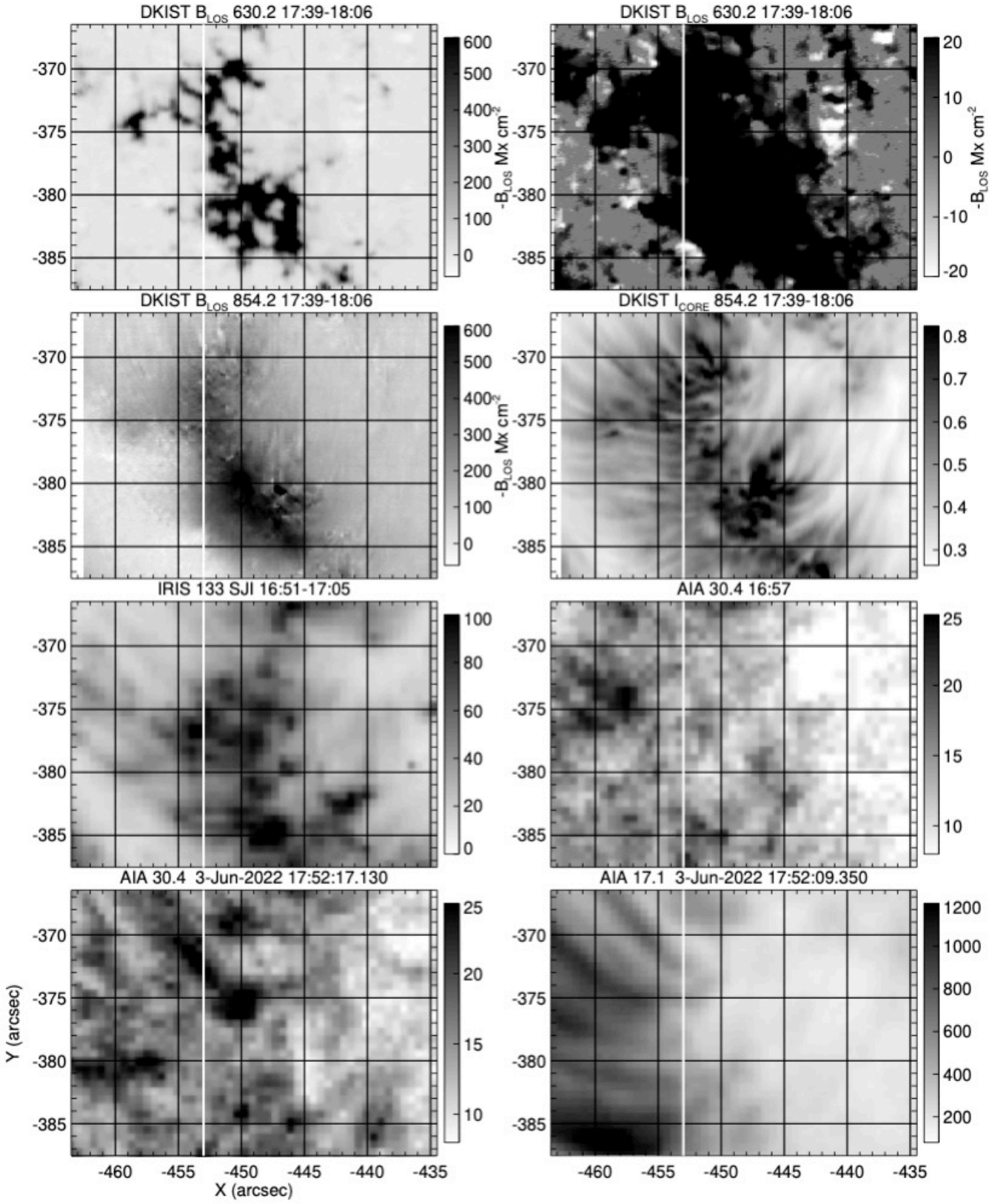

Figure 4. The eastern area of interest shown in Figure 2 is shown in DKIST data (upper two rows), slitjaw images at UV wavelengths from IRIS (third row), and AIA data (lower panels). IRIS data from 16:51 UT (in the third row) have been rotated to 17:52 UT, revealing the evolution over 1 hour of the 30.4 nm emission. Intensity data are in numbers of counts, except for the ViSP panel which is normalized to a continuum intensity of one. The white line marks the slice along which the line plots of Figure 5 are extracted. The upper right panel is a saturated version of the upper left panel.

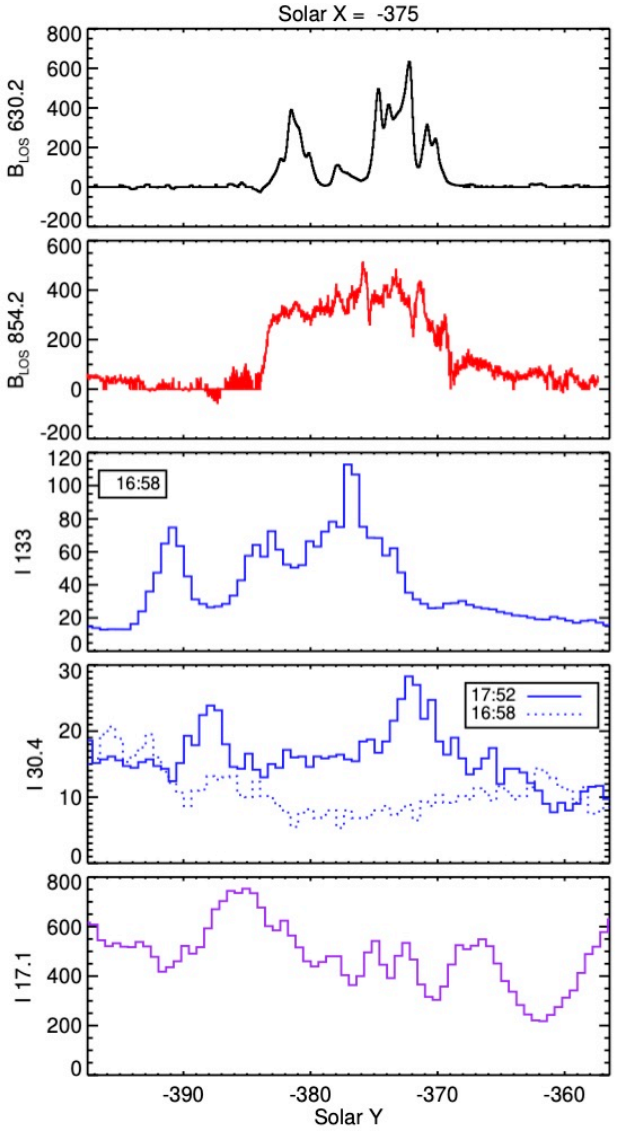

Figure 5. Line plots are shown of quantities extracted from the white line of Figure 4. The different colors correspond to different plasmas (black=photosphere, red=chromosphere, blue = transition region, purple=corona).

and we adopt a kinetic temperature T near 7000 K. For calcium $A = 40$ and $\sqrt{kT/Am_{\rm H}} = 1.2\ 10^5$ cm s^{-1}. The correction for the spectrograph PSF is given by s^2 where

$$s = \frac{1}{2\sqrt{\ln 2}}\,\frac{c}{\mathcal{R}} = 2.6\ 10^5 \quad \text{cm s}^{-1} \tag{2}$$

which is the 1σ width of the spectrograph PSF with resolution $\mathcal{R} = 69,000$. For pixels with widths $d\lambda = 0.00194$ nm, each pixel corresponds to a Doppler shift of $0.68\ 10^5$ cm s^{-1}.

Widths $w_{\rm LOS}$ for such a strong line as 854.2 nm, formed over many scale heights across the photosphere and chromosphere, present different challenges. Firstly the line is broadened not only by unresolved plasma motions (kinematics), but also by "opacity broadening," where photons trapped in the line core are occasionally shifted to wing wavelengths where they escape. This is tied to another basic difficulty in that the "width" of such a strong line, formed over several scale heights in the atmosphere, reflects conditions over the whole atmosphere from which photons escape to space. In the absence of a full "inversion", solving for atmospheric thermal and magnetic properties, we estimated non-thermal line widths in the upper chromosphere by using wavelength moments of the line depths (i.e., subtracting the line profiles from the continuum prior to calculating wavelength-weighted moments). Sobering systematic errors arising from inversions have been recently highlighted by Centeno et al. (2023, see their section 6), even for photospheric spectral lines. Such problems motivated our choice to use the far simpler, less accurate but perhaps more robust, WFA. Tests with Gaussian fits to the core revealed that the derived values reflect estimates of unresolved plasma motions in the upper chromosphere near and above 1400 km above the continuum photosphere (Cauzzi et al. 2008).

2.5. *Magnetic fields from DKIST data*

To derive magnetic fields from ViSP profiles, we used the weak field approximation (WFA, see Landi degl'Innocenti & Landolfi 2004) for both the pair of Fe I lines (630.15, 630.25 nm) as well as the Ca II 854.2 nm line. A photospheric line of Si I at 853.8015 nm within the 854.2 nm frames was also treated using the WFA, but only to confirm the close optical alignment between the 630 and 854 nm raster images obtained by ViSP. In the WFA we have, for magnetic fields along the line-of-sight $B_{\rm LOS}$ (Landi degl'Innocenti & Landolfi 2004; Centeno 2018),

$$V_\lambda = -\Delta\lambda_{\rm B}\,\bar{g}\cos\theta\,\frac{dI}{d\lambda} \tag{3}$$

where the Zeeman broadening parameter is

$$\Delta\lambda_{\rm B} = 4.6686\times10^{-11} B\,\lambda^2, \tag{4}$$

with λ in nm, and $\bar{g}$ is the effective Landé factor for each line (1.67, 2.5 and 1.1 for 630.15, 630.225 and 854.2 nm respectively). $B_{\rm LOS} = B\cos\theta$ was derived in several ways, the plots showing data from the ratio of integrals of V_λ and $dI/d\lambda$ over λ. However, following Kleint (2017), we also made a least-squares fit of V_λ to the numerical derivative of I to derive LOS magnetic flux densities to estimate uncertainties. RMS variations of the fits were found to be 1.2 and 8 Mx cm^{-2} for the 630.2 and 854.2 line respectively. These are larger than the 1σ random variations estimated using power spectra of spatial variations derived in Table 3 (see Figure 8).

For the magnetic field component in the plane of the sky (POS), and away from the line center wavelength

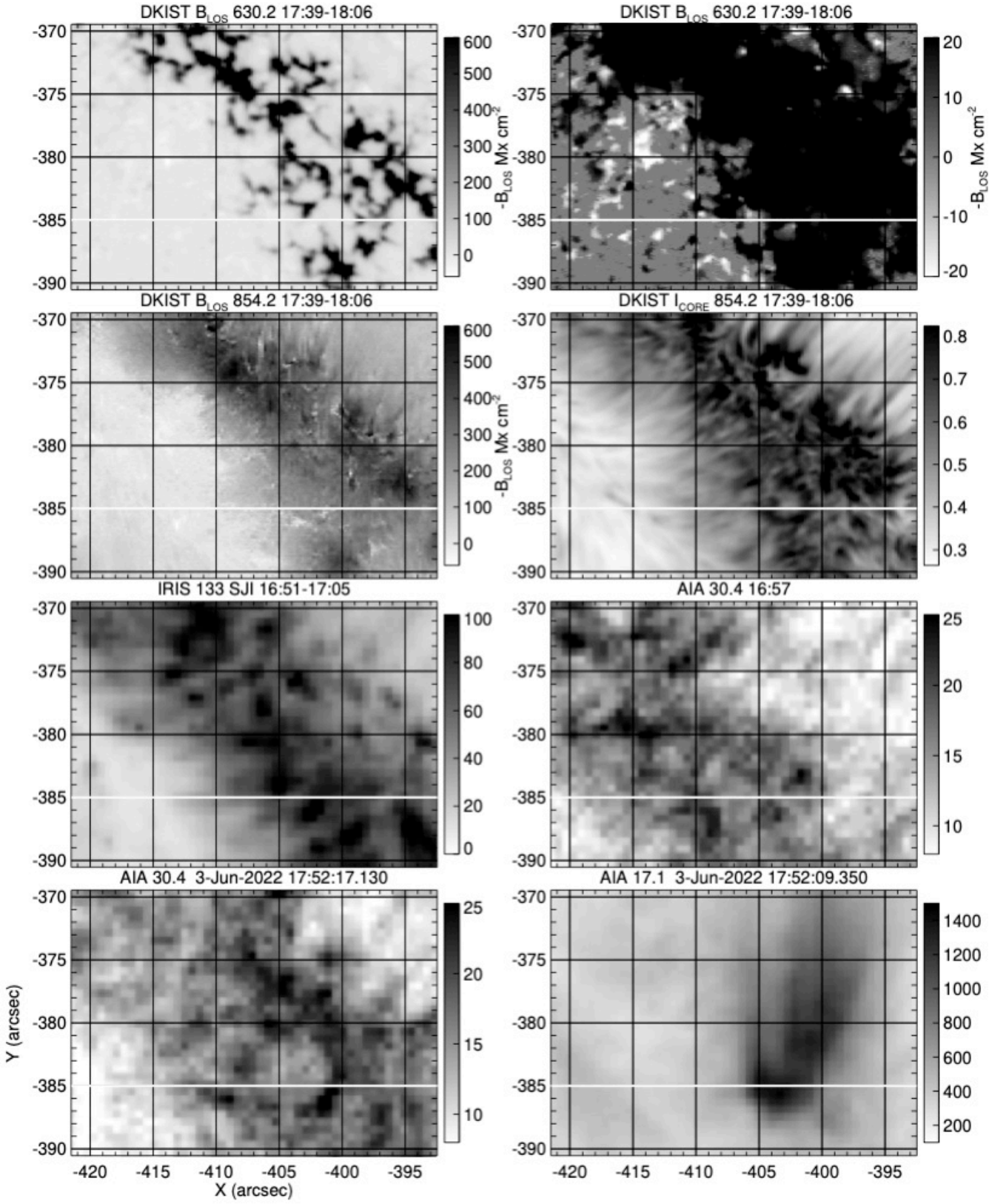

Figure 6. The western area of interest shown in Figure 2 is shown as in Figure 4. Again, data from 16:51 UT (in the third row) have been rotated to 17:52 UT, to show evolution of the AIA 30.4 nm channel over 1 hour. Notice the correspondence between the coronal footpoint centered at $X = -403, Y = -385$, and the near- contemporaneous ring-like structures in the core of the 854.2 chromospheric line and 30.4 nm emission line at 17:52:17 UT. The white line marks the slice along which the line plots of Figure 7 are extracted. The upper right panel is a saturated version of the upper left panel.

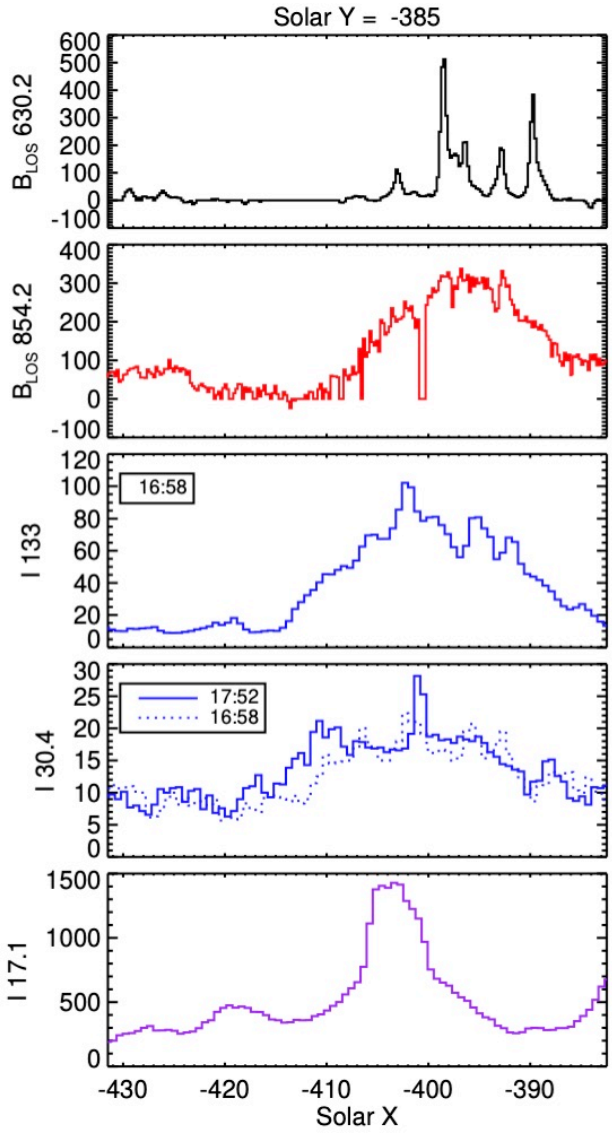

Figure 7. Line plots are shown of several quantities extracted from the white line of Figure 7.

λ_0, we have

$$P_\lambda = \sqrt{Q_\lambda^2 + U_\lambda^2} = \frac{3}{4}\,\Delta\lambda_B^2\,\bar{G}\sin^2\theta\,\frac{1}{\lambda-\lambda_0}\frac{dI}{d\lambda} \qquad (5)$$

where $\Delta\lambda_B$ is defined by B_{POS} instead of B_{LOS}, and $\bar{G}$ is the Landé factor for B_{POS} (Landi degl'Innocenti & Landolfi 2004), whose values for 630.15, 630.25 and 854.2 are are 3.29, 6.18 and 2.25 respectively. Again a least-squares fit of P_λ to the right-hand-side of equation (5) was used to derive B_{POS}. The azimuth of the magnetic field in the POS, χ, is given by

$$\frac{U_\lambda}{Q_\lambda} = \tan 2\chi \qquad (6)$$

with an ambiguity of 180°.

Table 3. Measured 1σ sensitivities to magnetic fields

Inst.	Line	B_{LOS}	Flux/ elem.	B_{POS}	Flux/ elem.
HMI	Fe I 617.3	2.7	3.6	...	...
ViSP	Fe I 630.2	0.7	0.15	2.3	0.5
ViSP	Ca II 854.2	2.5	0.6	44	10

Flux densities are in Mx cm^{-2}, fluxes per resolution element (Flux/elem.) are given in units of 10^{15} Maxwells. A "pixel length" of 0.2″ along the ViSP slit was adopted, multiplied by the slit width to find the approximate area of the effective resolution elements.

Subject to noise and sensitivity levels, these ViSP data probe the magnetic roots of the corona with a resolution in the solar X direction of ≈ 310 km. For simplicity, we will examine data as if it were acquired with square pixels of 0.″214 on each side. For each exposure, pixels along the slit of size 0.″0294 and 0.″0194 oversample these square pixels by the factors of f_y = 7.4 and 11 given above. After taking into account the modulation efficiency of the ViSP and the configuration-dependent beam imbalance (mainly caused by the grating polarization), the estimated polarimetric sensitivities are $\approx 1.2\times10^{-3}$ measured in the continuum. Binning by f_y =7 pixels along the slit, we estimate a sensitivity of $\approx 4\times10^{-4}$. This level is comparable to the best achieved with other grating spectropolarimeters (de la Cruz Rodríguez & Socas-Navarro 2011), smaller by a factor of roughly five than recent observations from an imaging spectropolarimeter (Esteban Pozuelo et al. 2023). The best polarization sensitivity is perhaps 10^{-5} obtained by the far-lower resolution ZIMPOL instrument (Povel 1995).

A polarization sensitivity of 4×10^{-4} per pixel at each spatial pixel translates to 1σ flux densities from equation (3) of 0.25 and 0.5 Mx cm^{-2} for the 630.2 and 854.2 lines respectively. These sensitivities were not, in practice, achieved (see Table 3). While the least-squares fits effectively integrate over several wavelength pixels, owing to non-ideal effects such as residual calibration errors, image motion, atmospheric perturbations and crosstalk, the measured sensitivities are larger.

The sensitivities of Table 3 were estimated by integrating white noise from spatial power spectra of pixels along the ViSP slit with the smallest signals (Figure 8). These include co-addition of multiple pixels along the slit and dispersion directions, roughly 25 co-added pixels for the 854.2 nm line. Therefore they should be compared with ideal values smaller by a factor of 5 than given above. We conclude that the ViSP instrument exhibited noise levels several times those estimated under ideal conditions.

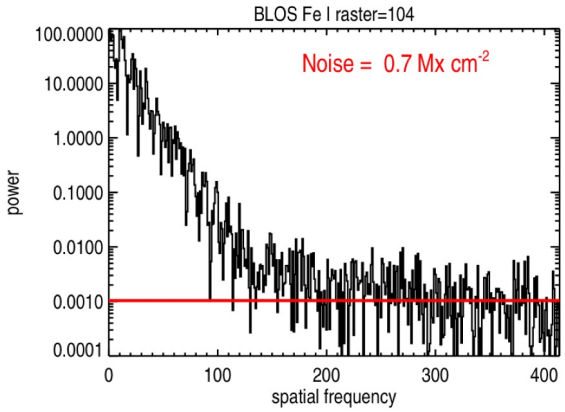

Figure 8. The power spectrum of spatial variations along the ViSP slit for raster 104. The noise is estimated by taking the square root of the sum of power underneath the red line. The point where the red line departs from the black near $X = 150$ is a measure of the smallest structure present in the data, whose Nyqvist sampling frequency is $\mathcal{N} = 0.5/0.059$ arcsec^{-1}. The spatial resolution along the slit is thus $\approx 1/(150\mathcal{N}/414) \approx 0\farcs3$, perhaps $0\farcs2$ for this particular power spectrum, depending on where the noise is considered as flat or "white".

The total unsigned flux from the WFA applied to the photosphere under the common area of overlap is

$$\Phi = a \sum_{\text{pixels}} \sqrt{B_{\text{LOS}}^2 + B_{\text{POS}}^2} \qquad (7)$$

with a the area of one pixel. Within the uncertainties the WFA fluxes given by equation (7) are equal in both the 630.2 and 854.2 lines, both yielding a flux of 6.0×10^{21} Mx. The line-of-sight flux of HMI is 1.7×10^{21} Mx compared with 2.0×10^{21} Mx for the ViSP 630.2 line. Given the level of accuracy of the WFA and the factor of at least two difference in angular resolution, this difference is neither surprising nor significant.

Vector magnetic fields from the WFA are shown in Figure 9, along with the rms speed ξ from equation (1). When multiplied by B^2 this leads to a quantity which is a crude upper limit on Poynting flux up into the corona (see section 3.3, shown in the lower left panel), in units of erg cm^{-2} s^{-1}. Clearly *this quantity from this particular region has little spatial correlation with the coronal emission*, or with emissions from plasma observed by IRIS or SDO.

The WFA signals in B_{LOS} in Figures 4 and 6 include detection of the fields in the chromospheric "canopy" (Giovanelli & Jones 1982). This is readily seen in the signals on either side of the ridges of intense chromospheric magnetic fields (the B_{LOS} panels of Figures 4 and 6). The diffuse fields to the north and west of the intense magnetic network are closer to Sun center than those to the south and east, and of opposite sign. This is exactly as expected as the fields become more horizontal farther from the network. Thus it seems that the coronal base has unipolar field extending across much larger areas than just the areas defined, say, by the more intense magnetic fields observed in the photosphere and chromosphere.

We also analyzed the other ViSP scans along with SDO and IRIS data obtained during the same campaign (Table 1). These all sampled mostly unipolar network regions associated with NOAA 13066, and were selected from more scans based upon the quality of ViSP quicklook images of granulation. The findings reported here for the BRWJV and AVORO data appear to be typical of all these datasets.

3. ANALYSIS

3.1. *Context and summary of observational results*

By themselves, the DKIST data offer little beyond what is known about chromospheric magnetic fields in relation to the lower atmosphere. For example, a recent similar study examined much quieter areas of the Sun's disk (Esteban Pozuelo et al. 2023), focusing on chromospheric magnetic fields alone. They found that, even in quiet regions of significant mixed polarity, larger areas of strong network are stable over at least 18 minutes, exhibiting little structure below $0.5''$ (refer to their Figure 10). In another relevant article, Chitta et al. (2017) related high resolution photospheric magnetic fields from the IMaX experiment (Martínez Pillet et al. 2011) on the second SUNRISE balloon mission (Solanki et al. 2017), to coronal loops, in a region of emerging magnetic flux. They concluded that

> "mixed polarity fields can be found at the base of coronal loops where magnetic flux cancellation events are possible"

and surmised that such bipolar regions may lie at the root of all coronal loops that were otherwise observed to be unipolar, at lower spatial resolutions.

The present paper differs in several ways. First it fills in the enormous gap between photospheric and coronal conditions by sampling plasmas across the entire atmosphere. Secondly we do not actively seek relationships between observed macroscopic features, Chitta et al. (2017) for example point to relations between chromospheric "anemones" and "X-ray jets" (Shibata et al. 2007). Chitta et al. (2017) related both of these phenomena to bipolarity in the underlying magnetic fields. This difference in approach may appear subtle, but our approach may help avoid the insidious issue of confirmation bias (Barker Bausell 2021). For example, along the dashed blue line highlighted in Figure 2 of Chitta et al. (2017), we see many coronal plasma loop footpoints which are not associated with bipolar features, and to some extent, *vice versa*.

On all scales, Figures 4 and 6 are rich in information. Both correlations and the lack of correlations are equally

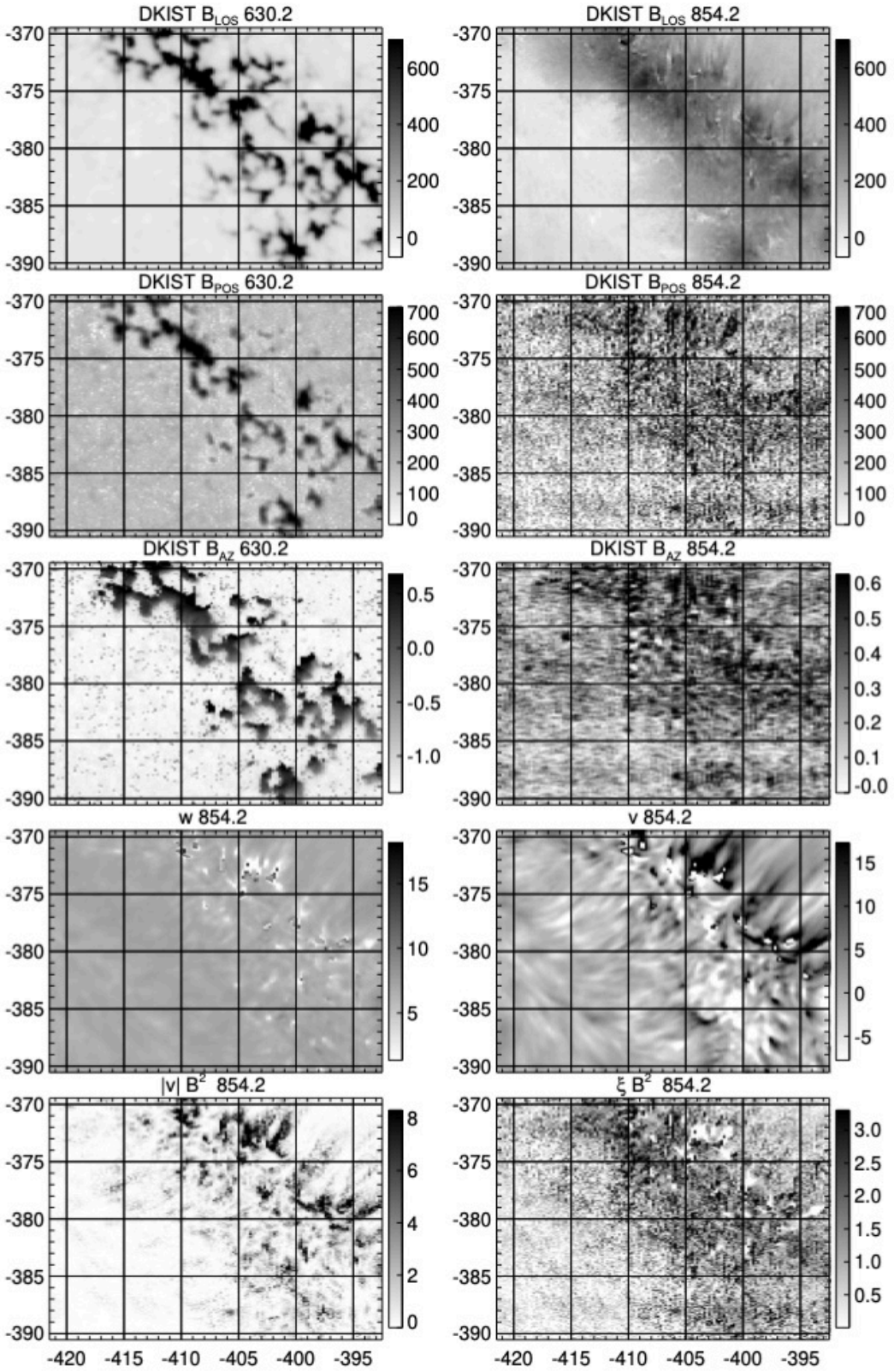

Figure 9. Components of the vector magnetic field derived from the weak field approximation of the 630.2 and 854.2 nm lines are shown, along with RMS velocities and the field amplitude $|B|$. The bottom panels show upper limits to the upward Poynting flux into the solar corona.

significant and important. The lack of correlations is a result that is robust against the relatively low accuracy of co-alignment between EUV and ground-based images (2-3″). Viewed within the current paradigm for coronal heating (section 1), these images open up a number of questions concerning the elementary structure of the solar atmosphere and corona in relation to magnetic fields emerging from beneath. There is no clear conflict between earlier work and our observational results. Instead our work brings together data from across the entire atmosphere, relating all evidence of plasma heating to properties of chromospheric magnetic fields and Poynting flux proxies.

Particularly striking in our study is the lack of correlation between magnetic fields, estimates of Poynting flux and overlying bright plasmas, when scrutinized on scales below the chromospheric network (1-20 Mm). Table 2 lists rank correlation coefficients from within the $12'' \times 12''$ area centered near the coronal footpoint seen in Figure 6. There is little correlation between variables when the coefficient is less than about 0.3 (as assessed using non-contemporaneous data, see the text in the Table). When computed over the $105'' \times 50''$ field of view, correlations between UV and EUV increase, revealing, as they should, the well-established correlations on large scales. But it is at and below these small scales that irreversible heating occurs, as expected from theory (Kuperus et al. 1981; Judge & Ionson 2023). Also, the utter lack of small-scale correlation of the EUV and UV data with photospheric magnetic fields is a sobering reminder of the difficulties faced when using photospheric magnetic fields alone to infer coronal properties, as has been common since the late 1960s (e.g. Altschuler & G. Newkirk 1969; Bale et al. 2019), and continued using far higher quality data by Chitta et al. (2017), among many others.

We can summarize more particular results which can be judged by inspection of our figures:

- Chromospheric vector magnetic fields are detected by the ViSP, not only over unipolar photospheric fields but also extending outwards across the interiors of network cells as a magnetic "canopy" (Giovanelli & Jones 1982).

- These extensions reach across and over areas of photospheric fields of opposite polarity lying beneath, consistent with expansion and volume-filling of the unipolar magnetic field in the upper chromosphere.

- Magnetic flux densities, and estimates of upper limits for Poynting fluxes, bear no obvious correlations with plasma radiating from the atmosphere above.

- Statistical correlations previously studied in lower resolution observations of photospheric magnetic fields and the overlying atmosphere begin to break down below scales of about 10 Mm (section 1).

Specific to images of the intensity of transition region lines, we find

- Bright emission exists only within strong unipolar chromospheric magnetic fields, and

- it is far weaker over the opposite polarity fields surrounding unipolar network boundaries in the photosphere.

- IRIS images in spectral lines of ions of C II (and Mg II and Si IV) differ radically from those of He II images from AIA, obtained simultaneously (Figures 4 and 6).

- Bright coronal emission arises from footpoints with almost no correlation with the IRIS and He II AIA images.

The last two points are most likely related to the documented failure of standard emission measure analysis to account for Li- and Na-like (Burton et al. 1971; Dupree 1972; Judge et al. 1995), and helium lines (Jordan 1975, 1980; Andretta & Jones 1997; Macpherson & Jordan 1999; Smith & Jordan 2002; Smith 2003; Judge & Pietarila 2004). As noted by Judge & Ionson (2023), transition region plasmas contain only a fraction of the mass even of the corona, so that their brightness is readily influenced by changes of mass, momentum and energy from both chromosphere and corona. It may be that the number of "discrepant" lines is large enough to question the general validity of underlying assumptions (Lang et al. 1990), particularly of the statistical equilibrium of plasma with electrons described by thermal distribution functions.

3.2. *Broader implications*

The radical differences measured between vector magnetic fields in the photosphere (broken-up, fractal-like structures) and chromosphere (smooth structures) imply that the chromosphere takes a primary role in determining the nature of the magnetic field and hence its free energy entering the corona. Qualitatively similar findings are readily seen in previously published work studying chromospheric magnetism (see, for example, Figure 1 of Socas-Navarro 2005 or Figures 5 and 13 of Anan et al. 2021). Thus, while not a new observational result, the main thrust of the present paper is to explore and emphasize previously unacknowledged consequences of this basic fact. We can also conclude that earlier work which has not included measurements of chromospheric magnetic fields, such as described in extensive reviews by Carlsson et al. (2019) and de Pontieu et al. (2021), has tended to focus upon thermal chromospheric fine structure and dynamics. This has diverted attention away from the coronal heating problem, which

primarily involves magnetic free energy, not the energy of ordered flows in the chromosphere *per se*.

Images of $B_{\rm LOS}$, derived from the chromospheric Ca II 854.2 nm line, are spatially smooth. They depart strongly with those of the line's core, velocity and width images (Figures 4, 6 and 9), forming in the upper-middle chromosphere (Cauzzi et al. 2008). The thermal fine structure is, in terms of force and energy balance, mostly a thermal "ornament" on a far less structured magnetic field which contains the bulk of the stress and energy density. Consequently, in the absence of routine measurements of magnetic fields threading through the chromosphere, it is not surprising that little progress has been made in identifying heating mechanisms of overlying, hotter plasmas.

The magnetic field measured from the WFA in the core of the Ca II 854.2 nm (formed near 1400 km in statically stratified models) is predominantly of a single polarity. The modest amount of opposite polarity photospheric magnetic flux has no signature in the chromospheric measurements. This novel result seems to deny models of overlying plasma heating based on multipolar fields over the observed regions. Such models include "cool loops" (Dowdy et al. 1986; Antiochos & Noci 1986; Hansteen et al. 2014), "tectonics" (Priest et al. 2002), and suggest that magnetic reconnection, if important, must occur only through tangentially discontinuous components of the vector field, with amplitudes far smaller than the strong guide field.

We must stress that our results do not apply to regions of active flux emergence or of mixed-polarity quiet Sun, but to the continued heating of long-lived, mostly unipolar network structures. Nevertheless here we have been able to refute an entire class of models for emission from the network and associated coronal loops. This kind of refutation is badly needed to make progress in plasma heating problems (Judge & Ionson 2023) given the current proliferation of ideas which have remained poorly challenged by critical observations.

Lastly, the strong correlations between coronal emission and photospheric magnetic field measurements stressed in the literature do not extend down to scales below a few Mm. Again this is not a new result, the question of why only certain bundles of flux contain brightly emitting plasma has been of concern for many years (Fort & Martres 1974; Bray et al. 1984; Litwin & Rosner 1993; Gurman 1993). As recognized by these authors and re-emphasized by Judge & Ionson (2023) and here, the implications regarding heating mechanisms are important and are discussed next.

3.3. *Physical connections from chromosphere to corona*

Ideally, as a first step to connect chromosphere and corona, we would measure the Poynting flux vector

$$\frac{1}{4\pi}(\mathbf{u}\times\mathbf{B})\times\mathbf{B} \equiv \frac{1}{4\pi}\left\{(\mathbf{B}\cdot\mathbf{u})\mathbf{B} - B^2\mathbf{u}\right\} \qquad (8)$$

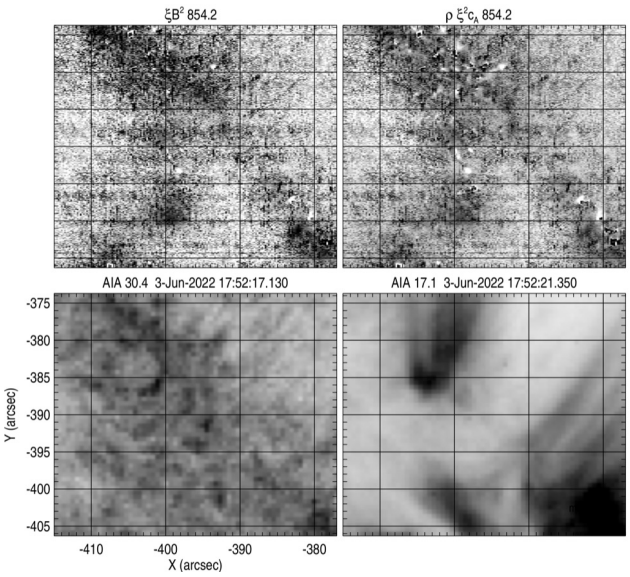

Figure 10. Relative Poynting flux estimates and AIA images are shown for dataset AVORO from 17:52, 3 June 2022.

to determine the energy flux directed upwards into the overlying plasmas. Below it will be convenient to write

$$\mathbf{B}(\mathbf{r},t) = \mathbf{B}_0(\mathbf{r}) + \mathbf{b}(\mathbf{r},t) \qquad (9)$$

where $\mathbf{B}_0(\mathbf{r})$ represents the large-scale observable field, averaged over time, and $\mathbf{b}(\mathbf{r},t)$ is the unobservable time-variable field associated with irreversible magnetic energy dissipation. Within the corona $\mathbf{B}_0$ may be close to a potential or force-free field, for example. Averaged over many dynamical times, $\langle\mathbf{b}\rangle = 0$, and $\langle\mathbf{B}\rangle = \mathbf{B}_0$.

The radiation losses from the chromosphere exceed those from the corona by at least an order of magnitude, in a real sense the corona is formed from the energy flux left over from heating the chromosphere. Therefore the energy flux from equation (8) should ideally be evaluated as close to the coronal base, i.e. the top of the chromosphere, as possible. Athay & White (1978) evaluated not the Poynting flux but the mechanical (acoustic) flux near the top of the chromosphere, showing that acoustic heating was insufficient to account for coronal heating in general.

In using equation (8), we must note that Zeeman measurements of $\mathbf{B}$ do not determine the sign of the field transverse to the line-of-sight. The second term of equation (8) is clearly unchanged under sign changes of any components of $\mathbf{B}$, but the first term is not. Therefore we cannot, even in principle, use the Zeeman effect to determine Poynting fluxes unless this transverse field ambiguity can be resolved by some means not contained in the Zeeman data themselves.

Worse still, $\mathbf{u}$ is also not determined through observations, instead we merely have the line-of-sight velocity shift $u_\parallel$ and the line width ξ. The nearest measurable quantities to the Poynting flux vector are just the scalar

quantities

$$v\,B^2/8\pi \quad \text{and} \tag{10}$$

$$\rho\,\xi^2 c_{\rm A}, \tag{11}$$

where ξ is interpreted as the amplitude of Alfvén waves, and $c_{\rm A} = B/\sqrt{4\pi\rho}$ is the group speed of the waves. It is easy to see the equivalence of equations (8) and (11) by noting that $\frac{1}{2}\rho\xi^2 = b^2/8\pi$ in an Alfvén wave, where b is the magnitude of the magnetic oscillation, propagating with group speed $c_{\rm A}$. Each of these crude "proxy" quantities clearly exceeds the magnitude of the actual Poynting flux available for heating, owing to the inequalities associated with the double vector product of equation (8), and the fact that the sign of the upward propagating flux is not known from the observables derived here. Nevertheless in Figure 10 we compare images of ξB^2 and $\rho\xi^2 c_{\rm A}$, as determined using the Ca II 854.2 nm line, with AIA 30.4 and 17.1 nm images. These images are gross over-estimates of the actual Poynting flux into the overlying corona from the chromosphere. The comparison is meaningful only in the limited and weak sense that if the actual Poynting fluxes are some fraction of the data plotted, and in the upward direction, then we should see correlations between coronal emission and these quantities. In comparing with coronal images there is no clear correlation.

These considerations might be pushed further by examining the individual images of the components of u, ξ, $B_{\rm LOS}$ and $B_{\rm POS}$ (Figure 9), which have their own particular spatial patterns. The (albeit noisy) components of vector magnetic fields over the magnetic network vary by less than a factor of 2 (Figure 9, 854.2 panels), loosely defining network as areas with $B_{\rm LOS}$ measured from Ca II above about 100 Mx cm^{-2}. Yet over these same regions the intensities of coronal emission vary by a factor of 6 or more (bottom panel of Figure 7). This suggests that whatever is heating the overlying corona, its signature is either not present in the data analyzed here, or that it lies in variations in the factor $\hat{\mathbf{B}}\cdot\hat{\mathbf{u}}$ in equation (8). This second case would seem to require peculiarly systematic changes in unit vector $\hat{\mathbf{u}}$, because observed variations across the observed area in $u_\parallel$, ξ and $\mathbf{B}$ are too small. Therefore we suggest that *there are processes outside of our current ability to measure, which determine the rate of coronal heating.* This point of view breaks from the common practice of seeking signatures in observable coronal phenomena (e.g. Peter et al. 2022).

Of several possible explanations, we might suggest (1) that the heating at EUV wavelengths is driven by conditions in the other footpoint, (2) that coronal heating occurs only beyond a certain (unknown) intrinsically critical level of heating (Litwin & Rosner 1993), and (3) that coronal heating cannot be treated merely as a consequence of lower boundary conditions, instead the heating is self-regulating, determining itself which bundles of flux are selected for enhanced heating (Einaudi et al. 2021). Case (1) seems statistically untenable because all the scans in Table 1 qualitatively show the same result (see, e.g., Figure 4), and we should have found at least some tighter correlations. If case (2) operates then the critical level does not correspond to anything magnetic on observable scales, implying either a dramatic role for unobserved (small-scale) variations in $\hat{\mathbf{u}}$, or for case (3) which has some support from numerical turbulence calculations (Einaudi et al. 2021). In this sense, the non-linearity implied by the critical level of heating suggested by Litwin & Rosner (1993) is perhaps just another, less general case of case (3).

The scalar proxy $\xi B^2 \approx 10^{10}$ erg cm^{-2} s^{-1} vastly exceeds the coronal energy requirements of $\lesssim 10^7$ erg cm^{-2} s^{-1} (Withbroe & Noyes 1977). This is readily understood, recalling that only the non-potential part of the magnetic field $\mathbf{B}$ contains energy that is free to provide heating. If, as implied in writing equation (9), $\mathbf{B}_0$ is merely a passive player in plasma heating (Sturrock 1999), then *a change in approach to the coronal heating problem is warranted,* since the conversion of free magnetic energy into heat involves only $\mathbf{b}(\mathbf{r},t)$, which is not directly observable. The only role for $\mathbf{B}_0$ is to fix large-scale topology and $c_{\rm A}$. If strong plasma heating depends critically on variables outside observational capabilities, it would then explain why correlations of $\mathbf{B}_0$ and derived quantities have led to inconclusive results (Fisher et al. 1998; Mandrini et al. 2000; Aschwanden 2001). Owing to fundamental challenges discussed in chapters 3 and 4 of Judge & Ionson (2023), there is no guarantee that such "hidden" variables will be revealed through more advanced observations. But suggestions for progress are given in chapter 5 in the same volume.

In the other proxy of Poynting flux $\frac{1}{2}\rho\xi^2 c_{\rm A}$, $\mathbf{B}_0$ enters only as the factor $c_{\rm A}$, and the free energy associated with b can be determined through the line widths and mass density. ξ is directly measured, ρ can be estimated from models, and $c_{\rm A}$ then estimated from the mesaured $\mathbf{B}_0$. Using $\rho = 3\times10^{-12}$ g cm^{-3} appropriate for the line core (Cauzzi et al. 2008), we find the more interesting energy flux density of $\approx 10^8$ erg cm^{-2} s^{-1}, a factor of ten above typical active-region energy losses. This number seems encouraging, suggesting that, whatever the nature of dissipation, energy estimates from observations and models might be not unrealistic.

We refute cool-loop models (Dowdy et al. 1986; Antiochos & Noci 1986) and any models relying on reconnection with opposite polarity fields (e.g., Priest et al. 2002) to provide heating to power the hot plasmas above. This is basically because the chromospheric magnetic flux beneath the bright EUV emission is unipolar. In an appendix, we show that invoking small-scale, unobserved flux of opposite sign to support cool loop models entails a logical *reductio ad absurdum.* The absence of correlations between plasma emission from $\approx 2\times10^4$, to several times 10^6 K suggests that the *observed* transition region plasma is not a thermal interface region associ-

ated with a relatively simple, locally unipolar field (as calculated explicitly in 2D by Gabriel 1976, for example). This argument echos conclusions derived by Feldman and colleagues based upon data with no magnetic field measurements or the highest resolution EUV data (Feldman 1983, 1987; Feldman & Laming 1993; Feldman 1998; Feldman et al. 2001). But our new measurements of chromospheric magnetic fields enable us to limit further the nature of plasma heating within the solar atmosphere. We conclude that the observed transition region plasmas are heated within locally unipolar magnetic structure by free energy associated with small-scale unresolved motions and/or non-potential magnetic fields. Intermittent current sheets generated by Parker's fundamental theorem of magnetostatics (Parker 1988, 1994), by MHD turbulence (Einaudi et al. 2021), or by internal surface waves (Ionson 1978) or phase mixed Alfvén waves in disordered plasmas (e.g., Howson et al. 2020) might fit the bill. Internal velocity shears generated by such dynamics might cause viscous ion heating (Hollweg 1985; Judge & Ionson 2023). But our essential result is that cool loops cannot account for transition region emission revealed by data obtained down to 0.214″pixels.

The intensities of lines of helium ions, formed in transition region plasmas, are anomalous (e.g. Jordan 1975, 1980; Andretta & Jones 1997; Macpherson & Jordan 1999; Smith & Jordan 2002; Smith 2003; Judge & Pietarila 2004). They are especially sensitive to such non-equilibrium physical processes (apparently diverse proposed processes were unified in the work of Pietarila & Judge 2004). The spatial and temporal differences between all the IRIS data and the He II AIA behavior, together with the well documented excess emission from helium lines suggest that helium emission is sensitive to high energy tails in particle and/or photon distribution functions, or perhaps long recombination times (Jordan 1980). The helium spectra, presenting a long-standing spectroscopic problem within transition region plasma, may ultimately shed more light on heating mechanisms in locally unipolar magnetic fields. It has been long recognized that the EUV helium lines are particularly large contributors to the formation of the ionosphere and its variability (Woolley & Allen 1948), yet the basic formation mechanisms within areas of active Sun remain poorly understood.

3.4. *A curious coronal footpoint*

In Figure 6 we noted a curious correspondence between the coronal footpoint centered at $X = -403, Y = -385$, and ring-like structures in the core of the 854.2 chromospheric line and 30.4 nm emission line from at 17:52:17 UT. The alignment of these images is accurate to $\approx 2-3''$ or better. No revised alignments within such uncertainties lead to better spatial correlations. However, if we were to assume that the nominal alignment is significant, then we can note interesting properties:

1. The underlying photospheric line of sight magnetic field shows no morphological resemblance to the overying radiating plasmas.

2. The chromospheric magnetic field directly underlying the structure (Figure 6) is of a uniform strength, lower than some of the neighboring fields. Hints of narrow opposite polarity fields (seen at $X = -404$ to -402, $Y = -386$ in Figure 6) are found to be artifacts from multi-peaked intensity profiles (see below).

3. Estimates of the magnitude of the Poynting flux (Figure 10) have no correlation with this feature.

The nature of the apparent structure is also guided by Stokes profiles $I_\lambda, Q_\lambda, U_\lambda, V_\lambda$ of the 854.2 nm measurements. The intensity (I_λ) profiles of 854.2 along the brighter ring all show extra emission in the core, leading to self-reversed profiles familiarly observed in the Ca II H and K lines (Linsky & Avrett 1970). The 854.2 nm V profiles across this area are consistent with the corresponding WFA (equation 3). Those hints of opposite polarity noted above are not physical, but artifacts of self-reversed I profiles. The region is entirely unipolar according to the 854.2 nm data.

The heated chromospheric and 30.4 nm plasmas appear as rings centered close to the coronal loop footpoint emission. The lack of any correlation between 30.4 and coronal emission indicates that this line of helium is more controlled by local plasma properties than optically thin illumination by radiation from the corona (Judge & Pietarila 2004, a property noted by). Instead, given the ring of 30.4 emission appearing to surround the 17.1 emission, we can speculate that the interface between the hot coronal loop's plasma and the surrounding plasma may play a role in generating extra heating via collisional *cross-field transport* processes, all within the same unipolar magnetic flux system. Cross-field processes have been previously studied (e.g. Athay 1990; Ji et al. 1996; Judge & McIntosh 2000; Ashbourn & Woods 2001; Judge 2008). (Ashbourn & Woods 2001) included a physical model for ion-acoustic turbulence to modify parallel and cross field transport. Perhaps there is also a role for local but non-Maxwellian particle distributions in the corona on scales of Mm, which are close to classical mean free paths of ions and electrons. Interestingly, the 30.4 nm emission of Figure 4 lies mostly *in between* regions of coronal emission, seen both as loop-like emission and in individual patches of 30.4 nm emission. While differential projection effects cannot be ruled out to explain these offsets, the offsets are in random directions which would be difficult to explain in the relatively homogeneous chromospheric magnetic field beneath.

4. CONCLUSIONS AND FURTHER SPECULATIONS

The present analysis suggests new avenues for making progress on a variety of puzzles involving magnetic plasma heating of the solar atmosphere. It may nevertheless appear superficially similar to earlier work, recent examples being Chitta et al. (2017); Anan et al. (2021); Esteban Pozuelo et al. (2023). We have taken special care to reduce and define uncertainties in co-alignment of diverse data across the entire atmosphere, from different instruments. The whole is greater than the sum of these components.

Our analysis also takes a broader view, deliberately stepping back to ask more elementary questions than is customary, based upon simple and obvious properties of the data, keeping firmly in mind the physical properties inferred from magnetic field measurements and elementary magneto-hydrodynamics. We have striven to minimize confirmation bias (Barker Bausell 2021) by analyzing every pixel in all data the same way, using cross correlations and power spectra, without by-eye selection of identifiable phenomena. From this more remote, and hopefully more objective viewpoint, we have suggested that several assumptions concerning coronal heating should be re-examined.

Uniquely, in stepping backwards and seeking to refute elementary predictions from physical models, we have shown that *measurable* (i.e. large-scale) magnetic fields contain little information on plasma heating, by themselves. Hot coronal plasmas form as a result of both external forcing *and* internal dynamics (Einaudi et al. 2021). Thus, the bright coronal plasmas observed seem to remain so as a result of "hidden", i.e. unobserved processes, which are internal to chromospheric and/or overlying plasmas themselves. We argue that the coronal plasma itself plays an active role in the heating mechanisms, chromospheric processes being of secondary importance. Theory would suggest that such a non-linearity should be expected. Highlighted recently by Judge & Ionson (2023), this view is along the same lines suggested independently by non-linear MHD calculations Einaudi et al. (2021):

> "Since the energy input is dependent on both the external forcing *and the internal dynamics*, the corona is a self-regulating forced system." (Our emphasis.)

This idea is not new, it is found in early models of 1D flows along flux tubes, prompted by the seminal work of Rosner et al. (1978). Kuin & Martens (1982); Martens & Kuin (1983) identified different attractor solutions, for the same physical ingredients, in analytical/numerical dynamical models with open connections to the chromosphere. The present analysis is perhaps *the first to* ***require*** *multiple solutions to explain the extreme variation of coronal heating, observed over a chromosphere whose measurable magnetic state is far more homogeneous.* This idea is also related to an earlier proposal for a "critical level" to be reached before significant coronal heating occurs (Litwin & Rosner 1993). A change in approaches to the coronal heating problem to accommodate this result therefore appears necessary, if only to try to refute it.

Our work begs further questions. Where is the lower temperature plasma emission arising from the conductive energy flux down from the corona? What is the physical nature of the plasmas observed at transition region temperatures? What is the role of departures from Maxwellian distributions within and between ions and electrons when mean free paths approach scales of macroscopic thermal structures (Jordan 1975; Judge & Ionson 2023)? It appears that whatever heats the bright EUV plasmas analyzed here must occur over locally unipolar chromospheric fields, in which the measurable field plays only a minor role in heating the plasma. This conclusion is in line with a series of arguments in the monograph by Judge & Ionson (2023). It follows an earlier argument in a prescient article by Sturrock (1999), that the magnetic fields *on measurable scales* play a passive role in coronal heating, serving mostly to set Alfvén speeds and topology more than determining plasma heating rates. If subsequently confirmed, this viewpoint explains why earlier statistical studies based upon observable magnetic fields ($\mathbf{B}_0$) have been largely inconclusive (Fisher et al. 1998; Mandrini et al. 2000; Aschwanden et al. 2000).

Lastly, we have inferred that bipolar fields measured in the photosphere have no role to play in heating the plasmas overlying the particular observed regions. Based only on SDO AIA images and HMI longitudinal photospheric magnetic fields, Tiwari et al. (2021) recently also concluded that bipolar fields are not *necessary* for heating coronal loops. Our conclusions are stronger: such configurations are *refuted* for the plasmas reported here.

APPENDIX

A. COOL LOOPS: REDUCTIO AD ABSURDUM

The cool loop proposal necessitates bipolar magnetic fields at scales $\lesssim$ 10 Mm (Dowdy et al. 1986; Antiochos & Noci 1986; Hansteen et al. 2014). Other models (Athay 1990; Ji et al. 1996; Ashbourn & Woods 2001, 2006; Judge 2008) require no bipoles, but they invoked a variety of processes related only to efficient "classical" rates of downward

heat conduction (Spitzer 1956; Braginskii 1965), and classical or turbulent cross-field transport processes. To survive scrutiny, the cool loop model must satisfy a minimum of four requirements

1. The loops must be observable at the UV and EUV wavelengths at which transition region plasma is regularly observed. These include lines of the Li- and Na- isolelectronic sequences from C IV at 155 nm down to lines of Be-like Ne VII at 46.5 nm, and Mg IX at 36.8 nm.

2. Opposite polarity footpoints of bipoles must either be observed, or shown to be compatible with available Zeeman measurements.

3. Loop-like structures between the footpoints must be responsible for the bulk of the transition region emission.

4. The number and nature of such loops must be able to account for the brightness of lines such as H Ly-α and from ions typically two to four times ionized.

The first requirement sets geometric constraints on the visibility of cool loops. Any proposed cool loops must extend about 0.8 Mm above the quiet continuum photosphere in order to be visible at wavelengths below 152 nm (Vernazza et al. 1981; Judge 2015, see also figures 8–11 of Skan et al. 2023, showing calculations for Si IV 139 and 140 nm lines). Spectral lines below 110 nm can only escape from regions 1.2 Mm above the photosphere. Smaller loops, which certainly exist, are however irrelevant to the interpretation of transition region emission. If loops are close to a potential state above the photosphere, they cannot extend much higher than the separation between their footpoints. MHD simulations of small loops show that this argument is reasonable outside of highly dynamic situations (Skan et al. 2023). No matter the sensitivity or angular resolution of any measurements, small bipoles with footpoints separated by $\lesssim$ 0.8–1.2 Mm statistically cannot easily contribute to observed cool loops. So the only question remaining is whether cool loops in the range of, say, 1–10 Mm can be consistent with measurements of magnetic fields from ViSP. The answer suggested by our analysis is no.

The fourth requirement has been shown to be false by Judge (2021) in several quieter IRIS datasets obtained near disk center and at the solar limb. The third is evidently refuted by comparing the top right images of photospheric $B_{\rm LOS}$ measurements in Figures 4 and 6, joining the opposite polarity (white) patches to neighboring dominant polarities, and looking to the bottom rows of both figures to see where emission occurs. There is no such correlation.

Our analysis reveals further problems with the notion of cool loops for the bright network regions targeted by DKIST. The domination of one polarity over the $105'' \times 50''$ common field of view, and its extension seen in HMI data, is extreme (compared with lower resolution measurements discussed by Giovanelli 1980): 97.5% of the detectable magnetic flux is negative, 2.1% positive. The upper right panels of Figures 4 and 6 show examples of small opposite-polarity flux concentrations outside of the primary polarity. The total flux of opposite polarity varies from the lower detection limit of $\approx 1.5 \times 10^{15}$ Mx in the 854.2 nm line (3 times the sensitivity level), up to the largest observed fluxes of 10^{19} Mx. *If the ViSP has resolved all the field present in the observations reported here* (i.e., there is no opposite polarity flux on scales below 150 km), then the measurements of $B_{\rm LOS}$ in the 630.2 and 854.2 nm lines in these figures reveal the sheer impossibility that loops returning within the vast, fairly uniform unipolar regions seen in the 854.2 magnetograms can exist. However, is it possible to hide opposite polarity flux in a physically meaningful manner?

It seems only one option is left to "save the phenomenon" of the cool loop picture. To account for the brightness of plasmas above the dominant unipolar network concentrations, we must hide tubes of magnetic flux beneath detection levels of $\approx 1.5 \times 10^{15}$ Mx with footpoints that must be separated by at least 1 Mm ($1\farcs4$). This means we must seek in the 854.2 magnetograms, formed 1400 km above the photosphere, signals of such concentrations which are associated with one end of a cool loop (the other being the dominant majority polarity). Close inspection of the figures show no significant correlation of this kind.

We can also bring a physical argument that the field *strengths* above a certain height in the chromosphere must be about the same magnitude owing to horizontal force balance. The measured unipolar flux densities in the 854.2 nm line generally exceed $B > 100$ Mx cm^{-2} over the network. Using the pressure at 1400 km from model C of Vernazza et al. (1981), the plasma $\beta = 8\pi p/B^2$ must satisfy $\beta < 0.005$. The associated Alfvén speed is $\gtrapprox 500$ km s^{-1}. Thus any magnetic field in the chromosphere no matter its sign, will quickly reach a field strength of at least 100 G, because no force can stop the magnetic field from filling space. With $B > 100$ G, flux $< 2 \times 10^{15}$ Mx, the tube area would not exceed 2×10^{13} cm^2. A cylindrical tube with this area would have a radius 25 km. If we add in one more constraint from observations, we will find bizarre unphysical properties of such cool loops. The emission measure in the lower transition region, averaged over much larger areas, is roughly 10^{27} cm^{-5} (Judge et al. 1995). That is, when averaged over areas S of several Mm^2, from which emission measures are derived from earlier observations, the average of $\int n_{\rm e}^2 dz$ is $\approx 10^{27}$ cm^{-5}. Assuming that this average applies roughly to the $105'' \times 50''$ area observed by DKIST (an area of 3×10^{19} cm^2, see Figure 2), we would require an average volumetric emission measure of $S \int n_{\rm e}^2 z \approx 3 \times 10^{46}$ cm^{-3}. With $n_{\rm e} \approx 10^{10}$ cm^{-3} a typical estimate of electron density, the emitting plasmas must fill a volume $V \approx 3 \times 10^{26}$

cm^3. If this is to be provided by cool loops of radius $< 2.5 \times 10^6$ cm, the total length of cool loops would need to exceed 1.5×10^{13} cm, over 210 solar radii or about 1 astronomical unit. Another way of saying this is that for each loop limited to being less than 10 Mm in order for them to be confined near the network boundaries, we would need $> 1.5 \times 10^7$ loops scattered across the DKIST common field of view of 3×10^{19} cm^2. If we further confine these to live within the network boundaries this would imply approximately 1 cool loop, of radius 25 km, every 10 meters across the length of network boundaries!

ACKNOWLEDGMENTS

This material is based upon work supported by the National Center for Atmospheric Research, which is a major facility sponsored by the National Science Foundation under Cooperative Agreement No. 1852977. PGJ is grateful to HAO Director Holly Gilbert for support of a research visit in Switzerland in 2023, to Daniela Lacatus for a thorough review of the article, and to Christian Beck and Gianna Cauzzi for their work acquiring the DKIST data and useful comments. Both the University of Bern and the International Space Science Institute supported this work, and grant No. 216870 from the Swiss Science Foundation to LK made this collaboration possible. The research reported herein is based in part on data collected with the Daniel K. Inouye Solar Telescope (DKIST), a facility of the National Solar Observatory (NSO). NSO is managed by the Association of Universities for Research in Astronomy, Inc., and is funded by the National Science Foundation. Any opinions, findings and conclusions or recommendations expressed in this publication are those of the authors and do not necessarily reflect the views of the National Science Foundation or the Association of Universities for Research in Astronomy, Inc. DKIST is located on land of spiritual and cultural significance to Native Hawaiian people. The use of this important site to further scientific knowledge is done so with appreciation and respect.

REFERENCES

Altschuler, M. D., & G. Newkirk, . J. 1969, Sol. Phys., 9, 131

Anan, T., Schad, T. A., Kitai, R., et al. 2021, ApJ, 921, 39, doi: 10.3847/1538-4357/ac1b9c

Andretta, V., & Jones, H. 1997, ApJ, 489, 375

Antiochos, S. K., & Noci, G. 1986, ApJ, 301, 440

Aschwanden, M. J. 2001, ApJ, 560, 1035, doi: 10.1086/323064

Aschwanden, M. J., & Nhalil, N. V. 2023, Frontiers in Astronomy and Space Sciences, 10, 1099346, doi: 10.3389/fspas.2023.1099346

Aschwanden, M. J., Nightingale, R. W., & Alexander, D. 2000, ApJ, 541, 1059

Ashbourn, J. M. A., & Woods, L. C. 2001, Proceedings of the Royal Society of London Series A, 457, 1873

—. 2006, A&A, 455, 1115, doi: 10.1051/0004-6361:20054400

Athay, R. G. 1990, ApJ, 362, 364, doi: 10.1086/169272

Athay, R. G., & White, O. R. 1978, ApJ, 226, 1135

Ayres, T. R. 2021, ApJ, 908, 205, doi: 10.3847/1538-4357/abd095

Bale, S. D., Badman, S. T., Bonnell, J. W., et al. 2019, Nature, 576, 237, doi: 10.1038/s41586-019-1818-7

Barker Bausell, R. 2021, The Problem with Science. The Reproducibility Crisis and What to Do About It (Oxford University Press)

Braginskii, S. I. 1965, Reviews of Plasma Physics., 1, 205

Bray, R. J., Loughhead, R. E., & Durrant, C. J. 1984, The Solar Granulation (Cambridge UK: Cambridge Univ. Press)

Burton, W. M., Jordan, C., Ridgeley, A., & Wilson, R. 1971, Phil. Trans R. Soc. London, A270, 81

Cally, P. S. 1990, ApJ, 355, 693

Carlsson, M., de Pontieu, B., & Hansteen, V. H. 2019, Ann. Rev. Astr. Astrophys., 57, 189

Cauzzi, G., Reardon, K. P., Uitenbroek, H., et al. 2008, A&A, 480, 515

Centeno, R. 2018, ApJ, 866, 89, doi: 10.3847/1538-4357/aae087

Centeno, R., Milić, I., Rempel, M., Nitta, N. V., & Sun, X. 2023, ApJ, 951, 23, doi: 10.3847/1538-4357/acd178

Chitta, L. P., Peter, H., & Young, P. R. 2021, A&A, 647, A159, doi: 10.1051/0004-6361/202039969

Chitta, L. P., Peter, H., Solanki, S. K., et al. 2017, ApJS, 229, 4, doi: 10.3847/1538-4365/229/1/4

Cook, J. W., & Ewing, J. A. 1990, ApJ, 355, 719

de la Cruz Rodríguez, J., & Socas-Navarro, H. 2011, A&A, 527, L8, doi: 10.1051/0004-6361/201016018

de Pontieu, B., Title, A. M., Lemen, J. R., et al. 2014, Sol. Phys., 289, 2733

de Pontieu, B., Polito, V., Hansteen, V., et al. 2021, Sol. Phys., 296, 84

de Wijn, A. G., Casini, R., Carlile, A., et al. 2022, Solar Phys., 297, 22

Doschek, G. A., Mariska, J. T., & Akiyama, S. 2004, ApJ, 609, 1153, doi: 10.1086/421235

Dowdy, J. F., J., Rabin, D., & Moore, R. L. 1986, Sol. Phys., 105, 35

Dupree, A. K. 1972, ApJ, 178, 527
Einaudi, G., Dahlburg, R. B., Ugarte-Urra, I., et al. 2021, ApJ, 910, 84
Esteban Pozuelo, S., Asensio Ramos, A., de la Cruz Rodríguez, J., Trujillo Bueno, J., & Martínez González, M. J. 2023, A&A, 672, A141, doi: 10.1051/0004-6361/202245267
Feldman, U. 1983, ApJ, 275, 367
—. 1987, ApJ, 320, 426
Feldman, U. 1998, ApJ, 507, 974
Feldman, U., Dammasch, I. E., & Wilhelm, K. 2001, ApJ, 558, 423
Feldman, U., & Laming, J. M. 1993, ApJ, 404, 799
Fisher, G. H., Longcope, D. W., Metcalf, T. R., & Pevtsov, A. A. 1998, ApJ, 508, 885
Fort, B., & Martres, M. J. 1974, A&A, 33, 249
Fox, N. J., Velli, M. C., Bale, S. D., et al. 2016, Space. Sci. Rev., 204, 7
Gabriel, A. 1976, Phil Trans. Royal Soc. Lond., 281, 339
Gallagher, P. T., Phillips, K. J. H., Harra-Murnion, L. K., & Keenan, F. P. 1998, A&A, 335, 733
Giovanelli, R. G. 1980, Sol. Phys., 68, 49
Giovanelli, R. G. 1982, Sol. Phys., 77, 27
Giovanelli, R. G., & Jones, H. P. 1982, Sol. Phys., 79, 267, doi: 10.1007/BF00146244
Gurman, J. B. 1993, ApJ, 412, 865
Hale, G. E., & Ellerman, F. 1904, ApJ, 19, 41
Hansteen, V., de Pontieu, B., Carlsson, M., et al. 2014, Science, 346, 1255757
Heyvaerts, J., & Priest, E. R. 1983, A&A, 117, 220
Hoeksema, J. T., Baldner, C. S., Bush, R. I., Schou, J., & Scherrer, P. H. 2018, Sol. Phys, 293, 45, doi: 10.1007/s11207-018-1259-8
Hollweg, J. V. 1985, JGR, 90, 7620, doi: 10.1029/JA090iA08p07620
Howard, R. 1959, ApJ, 130, 193, doi: 10.1086/146708
Howson, T. A., de Moortel, I., & Reid, J. 2020, A&A, 636, A40
Howson, T. A., de Moortel, I., Reid, J., & Hood, A. W. 2019, A&A, 629, A60, doi: 10.1051/0004-6361/201935876
Ionson, J. A. 1978, ApJ, 226, 650
Ji, H. S., Song, M. T., & Hu, F. M. 1996, ApJ, 464, 1012
Jordan, C. 1975, MNRAS, 170, 429
Jordan, C. 1980, Phil. Trans. R. soc. London, Series A, 297, 541
Judge, P., & Centeno, R. 2008, ApJ, 687, 1388
Judge, P. G. 2008, ApJL, 683, L87
Judge, P. G. 2015, ApJ, 808, 116
—. 2021, ApJ, 914, 70
Judge, P. G., & Ionson, J. A. 2023, The Problem of Coronal Heating. A Rosetta Stone for Electrodynamic Coupling in Cosmic Plasma (Springer, in press)
Judge, P. G., & McIntosh, S. 2000, Sol. Phys., 190, 331
Judge, P. G., & Pietarila, A. 2004, ApJ, 606, 1258
Judge, P. G., Woods, T. N., Brekke, P., & Rottman, G. J. 1995, ApJL, 455, L85
Kleint, L. 2017, ApJ, 834, 26
Kuin, N. P. M., & Martens, P. C. H. 1982, A&A, 108, L1
Kuperus, M., Ionson, J. A., & Spicer, D. S. 1981, A&A, 19, 7
Landi degl'Innocenti, E. L., & Landolfi, M. 2004, Astrophysics and Space Library, Vol. 307, Polarization in Spectral Lines (Dordrecht: Kluwer Academic Publishers)
Lang, J., Mason, H. E., & McWhirter, R. W. P. 1990, Sol. Phys., 129, 31
Leighton, R. B. 1959, ApJ, 130, 366
Lemen, J. R., Title, A. M., Akin, D. J., et al. 2012, Sol. Phys., 275, 17, doi: 10.1007/s11207-011-9776-8
Linsky, J. L., & Avrett, E. H. 1970, PASP, 82, 169
Lites, B. W. 1987, Applied Optics, 26, 3838
Litwin, C., & Rosner, R. 1993, ApJ, 412, 375
Loukitcheva, M., Solanki, S. K., & White, S. M. 2009, A&A, 497, 273, doi: 10.1051/0004-6361/200811133
Macpherson, K., & Jordan, C. 1999, MNRAS, 308, 510
Mandrini, C. H., Démoulin, P., & Klimchuk, J. A. 2000, ApJ, 530, 999
Mariska, J. T. 1992, The Solar Transition Region (Cambridge UK: Cambridge Univ. Press)
Martens, P. C. H., & Kuin, N. P. M. 1983, A&A, 123, 216
Martinez-Galarce, D. S., Walker, Arthur B. C., I., Barbee, Troy W., I., & Hoover, R. B. 2003, ApJ, 585, 1095, doi: 10.1086/345496
Martínez Pillet, V., del Toro Iniesta, J. C., Álvarez-Herrero, A., et al. 2011, Sol. Phys., 268, 57, doi: 10.1007/s11207-010-9644-y
Mok, Y., & Einaudi, G. 1990, ApJ, 351, 296, doi: 10.1086/168465
Neupert, W. M. 1998, Sol. Phys., 177, 181, doi: 10.1023/A:1004999909066
Parker, E. N. 1988, ApJ, 330, 474
—. 1994, Spontaneous Current Sheets in Magnetic Fields with Application to Stellar X-Rays, International Series on Astronomy and Astrophyics (Oxford: Oxford University Press)
Parnell, C. E., & de Moortel, I. 2012, Royal Society of London Philosophical Transactions Series A, 370, 3217. https://arxiv.org/abs/1206.6097
Pesnell, W. D., Thompson, B. J., & Chamberlin, P. C. 2012, Sol. Phys., 275, 3

Peter, H., Chitta, L. P., Chen, F., et al. 2022, ApJ, 933, 153, doi: 10.3847/1538-4357/ac7219
Pietarila, A., & Judge, P. G. 2004, ApJ, 606, 1239
Pontin, D. I., & Priest, E. R. 2022, Living Reviews in Solar Physics, 19, 1
Povel, H.-P. 1995, Optical Engineering, 34, 1870, doi: 10.1117/12.200596
Priest, E. R., Heyvaerts, J. F., & Title, A. M. 2002, ApJ, 576, 533
Rappazzo, A. F., Velli, M., Einaudi, G., & Dahlburg, R. B. 2008, ApJ, 677, 1348, doi: 10.1086/528786
Reeves, E. M. 1976, Sol. Phys., 46, 53
Rimmele, T. R., Warner, M., Keil, S. L., et al. 2020, Sol. Phys., 295, 172, doi: 10.1007/s11207-020-01736-7
Rosner, R., Tucker, W. H., & Vaiana, G. S. 1978, ApJ, 220, 643
Schmelz, J. T., & Winebarger, A. R. 2015, Philosophical Transactions of the Royal Society A: Mathematical, Physical and Engineering Sciences, 373, 20140257, doi: 10.1098/rsta.2014.0257
Schrijver, C. J. 1987, A&A, 180, 241
Schrijver, C. J. 1988, A&A, 189, 163
Schrijver, C. J., & Harvey, K. L. 1989, ApJ, 343, 481
Schrijver, C. J., & Title, A. M. 2003, ApJL, 597, L165
Schrijver, C. J., Zwaan, C., Maxson, C. W., & Noyes, R. W. 1985, A&A, 149, 123
Schrijver, C. J., Title, A. M., Harvey, K. L., et al. 1998, Nature, 394, 152, doi: 10.1038/28108
Shibata, K., Nakamura, T., Matsumoto, T., et al. 2007, Science, 318, 1591, doi: 10.1126/science.1146708
Skan, M., Danilovic, S., Leenaarts, J., Calvo, F., & Rempel, M. 2023, A&A, 672, A47, doi: 10.1051/0004-6361/202245390
Skogsrud, H., Voort, L. H. M. R. V. D., & Pontieu, B. D. 2015, ApJ, 817
Smith, G. R. 2003, MNRAS, 341, 143
Smith, G. R., & Jordan, C. 2002, MNRAS, 337, 666
Socas-Navarro, H. 2005, ApJL, 631, L167
Solanki, S. K., Riethmüller, T. L., Barthol, P., et al. 2017, ApJS, 229, 2, doi: 10.3847/1538-4365/229/1/2
Spitzer, L. 1956, Physics of Fully Ionized Gases (New York: Interscience Publishers)
Sturrock, P. A. 1999, ApJ, 521, 451, doi: 10.1086/307544
Tiwari, S. K., Evans, C. L., Panesar, N. K., Prasad, A., & Moore, R. L. 2021, ApJ, 908, 151, doi: 10.3847/1538-4357/abd176
Toriumi, S., & Airapetian, V. S. 2022, ApJ, 927, 179, doi: 10.3847/1538-4357/ac5179
Vernazza, J. E., Avrett, E. H., & Loeser, R. 1981, ApJS, 45, 635
Withbroe, G. L., & Noyes, R. W. 1977, Ann. Rev. Astr. Astrophys., 15, 363
Woolley, R. D. V. R., & Allen, C. W. 1948, MNRAS, 108, 292